PHYSICAL REVIEW E **109**, 025105 (2024)

Nanoscale electrohydrodynamic ion transport: Influences of channel geometry and polarization-induced surface charges

Arghyadeep Paul [1] and N. R. Aluru [2]

[1] *Department of Mechanical Science and Engineering, Beckman Institute for Advanced Science and Technology, University of Illinois at Urbana–Champaign, Urbana, Illinois 61801, USA*

[2] *Walker Department of Mechanical Engineering, Oden Institute for Computational Engineering and Sciences, The University of Texas at Austin, Austin, Texas 78712, USA*

(Received 23 August 2023; accepted 19 January 2024; published 21 February 2024)

Electrohydrodynamic ion transport has been studied in nanotubes, nanoslits, and nanopores to mimic the advanced functionalities of biological ion channels. However, probing how the intricate interplay between the electrical and mechanical interactions affects ion conduction in asymmetric nanoconduits presents further obstacles. Here, ion transport across a conical nanopore embedded in a polarizable membrane under an electric field and pressure is analyzed by numerically solving a continuum model based on the Poisson, Nernst-Planck, and Navier-Stokes equations. We report an anomalous ionic current depletion, of up to 75%, and an unexpected rise in current rectification when pressure is exerted along the external electric field. Membrane polarization is revealed as the prerequisite to obtain this previously undetected electrohydrodynamic coupling. The electric field induces large surface charges at the pore tip due to its conical shape, creating nonuniform electrical double layers (EDL) with a massive accumulation of electrolyte ions near the orifice. Once applied, the pressure distorts the quasiequilibrium distribution of the EDL ions to influence the nanopore conductivity. Our fundamental approach to inspect the effect of pressure on the channel EDL (and thus ionic conductance) in contrast to its effect on the current arising from the hydrodynamic streaming of ions further explains the pressure-sensitive ion transport in different nanochannels and physical regimes manifested in past experiments, including the hitherto inexplicit mechanism behind the mechanically activated ion transport in carbon nanotubes. This enhances our broad understanding of nanoscale electrohydrodynamic ion transport, yielding a platform to build nanofluidic devices and ionic circuits with more robust and tunable responses to electrical and mechanical stimuli.

DOI: 10.1103/PhysRevE.109.025105

I. INTRODUCTION

Lately, electrohydrodynamic ion transport [1–7] has gained a great deal of attention in nanofluidics to mimic the characteristics of biological ion channels [8–11]. Although a plethora of exotic fluid and ion transport phenomena [1–4,12–21] are displayed in artificial nanoscale conduits [2,13,22–28], they are yet to replicate the advanced responses of their biological counterparts to electrical, mechanical, and chemical stimuli, which engender intricate functionalities such as highly selective [11], mechanosensitive [8–10], and voltage-gated [8,11] ion conduction. Over the last decade, ion transport under coupled voltage and pressure drops has been explored mostly in uniformly shaped nanoconfinements like graphene nanoslits [2], carbon nanotubes [3], and graphene nanopores [4]. Consequently, investigating the electrohydrodynamic ion transport under similar circumstances in nanochannels with an asymmetric geometry [29–31] such as a conical nanopore [31–41] naturally presents the next frontier in the field.

Solid-state nanopores [41–47] offer a versatile platform to explore nanoscale ion transport for applications such as biosensing [46–57], drug delivery [57,58], and chemical separation [46,59–61]. The characteristics of ionic motion within such channels are directed by the properties of the electrical double layers (EDL) formed on their charged surfaces [45]. The asymmetric structure of a conical nanopore generates uneven EDL overlaps along its length [31,34], resulting in intriguing phenomena like ionic concentration polarization (ICP) [62–66], ionic current rectification (ICR) [31–40], and ion selectivity [40,67–69]. However, when embedded in a dielectric membrane, the conical shape of a nanopore has added ramifications due to induced charge effects (ICE) [70–75]. Induced surface charges are generated by the polarization of a dielectric material in response to an external electric field, which creates an uneven charge distribution on the lateral surface of a solid-state conical nanopore and redistributes the surrounding electrolyte ions into forming a nonuniform EDL [36,37]. When applied, a pressure additionally deforms the quasiequilibrium EDL structure due to hydrodynamic flow, further altering the electrokinetic properties in the nanopore [4–7].

While analyzing nanoscale ion transport under coexisting electric field and pressure, Marcotte *et al.* [3] found mechanically activated ionic current in single-digit carbon nanotubes (CNTs) with the conductance depending quadratically on pressure and implied the low friction encountered by water inside the CNT to be responsible for it. Jiang *et al.* [4] also illustrated a symmetric but linear variation of the ionic conductance in graphene nanopores with pressure. Meanwhile, in graphene nanoslits, Mouterde *et al.* [2] inferred the large

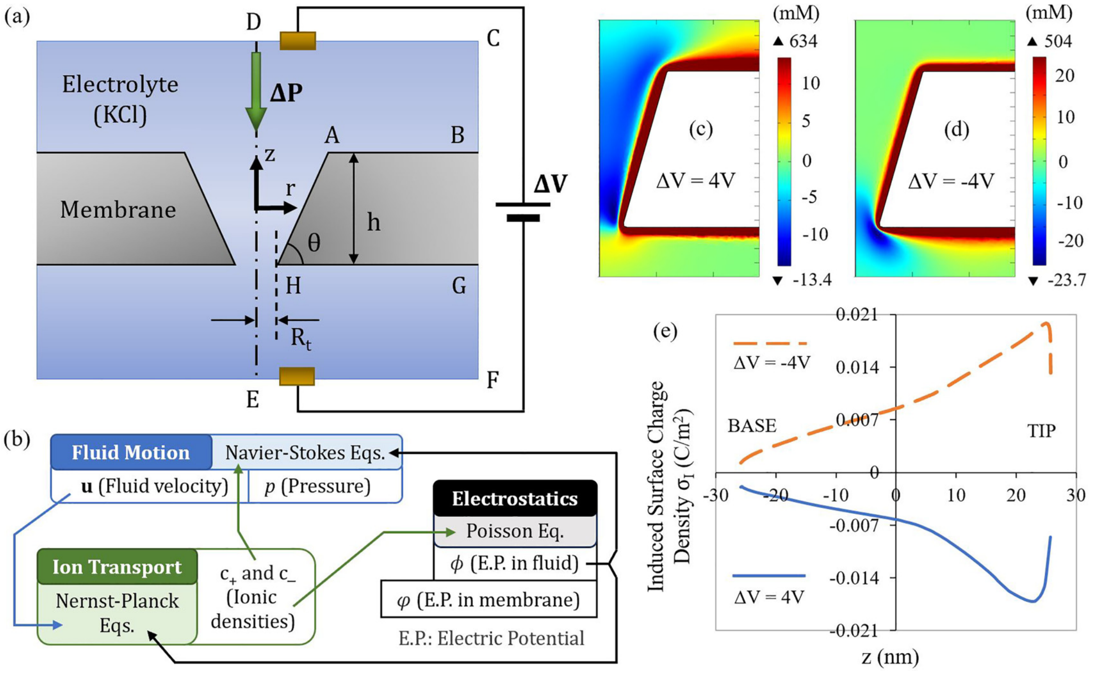

FIG. 1. (a) A cross section of a conical nanopore embedded in a dielectric membrane separating two KCl electrolytic reservoirs is shown in the cylindrical coordinates (r, z). A voltage ΔV and pressure ΔP are applied in the negative-z direction. (b) A chart illustrates the equations considered to study the ion transport across the nanopore, their dependent variables, and the exchange of the variables needed between them. At $\Delta P = 0$, $\sigma = -0.03\,\mathrm{C/m^2}$, $\varepsilon = 12$, $R_t = 8$ nm, $h = 55$ nm, $\theta = 74^\circ$, and $c_0 = 35$ mM, (c) and (d) display 2D contours of the net ionic concentration ($c_+ - c_-$) for $\Delta V = 4$ V and -4 V, respectively, while (e) evaluates the distribution of induced surface charge density (σ_I) on the nanopore sidewall (AH) using Eq. (4b).

hydrodynamic slip on graphene to be at the root of a quadratic gating of the (pressure-driven) streaming current with applied voltage. Albeit analogous studies have been carried out in conical nanopores, which report a bidirectional pressure-induced reduction of ICR [5–7], none of them considered ICE as the phenomenon is usually significant in atomically thin membranes [76]. However, in a solid-state conical nanopore, the inevitable low membrane thickness near the orifice yields substantial polarization [36,37] even if the membrane itself is not thin away from the pore opening [36], a situation where ICE cannot be overlooked. Nonetheless, the impact of polarization-induced surface charges on the ion transport characteristics in a conical nanopore under coupled electrohydrodynamic actuation remains unexplored.

Here, we study the ion transport across a conical nanopore embedded in a dielectric membrane between two electrolytic reservoirs under an electric field and pressure. Numerical simulations of a continuum model based on the Poisson, Nernst-Planck, and Navier-Stokes equations reveal an unexpected electrohydrodynamic coupling that suppresses ionic flux and raises ICR if pressure is applied along the electric field. Such observations are explained by the distribution of ionic density across the nanopore, prior to and after the application of pressure, which demonstrate the hydrodynamic displacement of its EDL ions from their quasiequilibrium positions to help characterize the change in ionic conductance. Conditions boosting the anomalous pressure-induced reduction of conductance are also explored. Furthermore, we illustrate that comparing how pressure alters the voltage-driven current (by distorting the channel EDL to influence the ionic conductance) and the streaming current engendered by the hydrodynamic flux of ions can help resolve the mechanism behind the pressure-modulated ion transport in various nanochannels, including that in narrow single-digit CNTs (which was unclear). Hence, we propose this as a fundamental strategy to predict the electrohydrodynamic ion transport features in nanoconduits and that our analysis can help build nanofluidic devices manifesting an improved control over molecular and ion transport.

II. SYSTEM DESCRIPTION

Figure 1(a) depicts a truncated-conical nanopore within a polarizable membrane of dielectric constant ε. The nanopore is axisymmetric about its centerline DE (coinciding with the z axis) and its center lies on the origin of the cylindrical coordinates (r, z), due to which the half-section space enclosed by the segment $CDEF$ is sufficient to be used as the system for the numerical simulations employed to study ion transport across the pore (detailed in Sec. III). The membrane separates two reservoirs filled with KCl solution of bulk salt concentration c_0, with the ionic diffusion coefficients $D(\mathrm{K^+}) = 1.95 \times 10^{-9}\ \mathrm{m^2/s}$ and $D(\mathrm{Cl^-}) = 2.03 \times 10^{-9}\ \mathrm{m^2/s}$. We consider the electrolytic solution to have a dielectric constant $\varepsilon_f = 80$, a density $\rho = 1000\,\mathrm{kg/m^3}$, and a viscosity $\eta = 1$ mPa s. The system temperature is assumed constant at $T = 298$ K. The nanopore geometry is dictated by the tip radius R_t, the complementary cone angle θ, and the pore length h. The pore end with the smaller (larger) opening is referred to as the tip (base) side. The nanopore sidewall (AH) and membrane surfaces (AB

and *HG*) carry a uniform inherent surface charge density σ (considered as negative throughout the paper) prior to polarization. An electric potential difference ΔV and a pressure differential ΔP are applied on the top reservoir relative to the bottom reservoir. As a positive ΔV or ΔP generates a downward ionic current (I), I is taken as positive in the negative-z direction. The fluid and membrane domains are enclosed by segments *ABCDEFGH* and *BAHG*, respectively.

III. MATHEMATICAL MODEL AND METHODS

A. Electrostatics

The electric potential in the fluid domain ϕ is governed by the Poisson equation:

$$-\varepsilon_0\varepsilon_f\nabla^2\phi = e(c_+ - c_-), \tag{1}$$

where ε_0 is the electric permittivity in vacuum, e is the elementary charge, and c_+ and c_- are the ionic concentrations of K^+ and Cl^-, respectively. The right-hand side of Eq. (1) represents the net local volumetric charge density of mobile ions in the fluid. But, since mobile ions are absent in dielectric materials, the electric potential in the membrane domain φ is mediated by the Laplace equation,

$$\nabla^2\varphi = 0. \tag{2}$$

As the electric potential of the top reservoir is ΔV relative to that of the bottom reservoir, we impose

$$\phi_{\mathrm{DC}} = \Delta V/2 \text{ and } \phi_{\mathrm{EF}} = -\Delta V/2. \tag{3}$$

The radial gradients of ϕ and φ are significant only in the vicinity of the pore as the transmembrane electric potential difference ΔV is applied in the axial direction. As a result, the radial component of electric field is absent on *CB*, *BG*, and *GF* (distant from the pore). At the fluid-membrane interfaces (*AB, AH*, and *HG*), the electric potential is continuous, $\phi = \varphi$, and their gradients are related as

$$\mathbf{n}\cdot(-\varepsilon_0\varepsilon_f\nabla\phi) + \mathbf{n}\cdot(\varepsilon_0\varepsilon\nabla\varphi) = \sigma, \tag{4a}$$

$$\mathbf{n}\cdot(-\varepsilon_0\varepsilon_f\nabla\phi) = \sigma_N = \sigma + \sigma_I \Rightarrow \sigma_I = -\mathbf{n}\cdot(\varepsilon_0\varepsilon\nabla\varphi), \tag{4b}$$

where $\mathbf{n}$ is the unit vector normal to the fluid-membrane interface pointing into the fluid domain. While the electric fields in the electrolyte ($-\nabla\phi$) drive the ionic motion, the electric fields in the membrane ($-\nabla\varphi$) arising from its dielectric polarization induce additional charges on the pore and membrane surfaces. Thus, the term $\mathbf{n}\cdot(\varepsilon_0\varepsilon\nabla\varphi)$, accounting for the latter, captures ICE. As a surface with net charge density σ_N (i.e., the sum of σ and the induced surface charge density σ_I) produces an electric field of $\mathbf{n}\cdot(-\nabla\phi) = \sigma_N/(\varepsilon_0\varepsilon_f)$ to its normal direction in the fluid domain, substituting $\mathbf{n}\cdot(-\varepsilon_0\varepsilon_f\nabla\phi) = \sigma_N$ in Eq. (4a) yields $\sigma_I = -\mathbf{n}\cdot(\varepsilon_0\varepsilon\nabla\varphi)$ in Eq. (4b).

B. Fluid transport

Fluid motion is taken into account using the Navier-Stokes (NS) equations:

$$\nabla\cdot\mathbf{u} = 0, \tag{5}$$

$$\rho[\mathbf{u}\cdot\nabla\mathbf{u}] = -(\nabla \mathrm{p}) + \eta(\nabla^2\mathbf{u}) - e(c_+ - c_-)\nabla\phi. \tag{6}$$

Here, $\mathbf{u}$ is the fluid velocity, p is the pressure, and $-e(c_+ - c_-)\nabla\phi$ is the electrostatic force acting on the fluid, while the inertial term $\rho[\mathbf{u}\cdot\nabla\mathbf{u}]$ can also be neglected due to the typically low Reynolds numbers in nanofluidics. We apply a pressure ΔP at the inlet *DC* relative to the outlet *EF*,

$$\mathrm{p}_{\mathrm{DC}} = \Delta P/2 \text{ and } \mathrm{p}_{\mathrm{EF}} = -\Delta P/2. \tag{7}$$

Additionally, we set the shear stress in the tangential (radial) direction at the inlet and outlet to be zero. No-slip and no-penetration boundary conditions are applied at the fluid-membrane interfaces (*AB, AH*, and *HG*). Lastly, we impose the zero shear stress and zero radial fluid velocity boundary conditions on *CB* and *GF* [37,77], as they only depict suitable limits of the computational domain sufficiently far away from the pore beyond which the gradients of all the variables are insignificant; the actual reservoir walls are much farther away from the pore and essentially irrelevant here.

C. Ion transport

Ionic motion in the fluid is directed by the Nernst-Planck (NP) equations:

$$\nabla\cdot\mathbf{J}_\pm = 0, \tag{8}$$

$$\mathbf{J}_\pm = \mathbf{u}c_\pm - D_\pm\nabla c_\pm - \left[\pm\frac{D_\pm}{k_B T}ec_\pm\nabla\phi\right], \tag{9}$$

where k_B is the Boltzmann constant, $\mathbf{J}_\pm$ is the ionic flux, and the terms in Eq. (9) are its advection, diffusion, and electromigration components, respectively. Simply put, the NP equations conserve the individual ionic species. We set a zero normal ionic flux on the fluid-membrane interfaces, and also on *CB* and *GF* as they are far away from the pore. Finally, at the reservoirs,

$$(c_\pm)_{\mathrm{DC}} = c_0 \text{ and } (c_\pm)_{\mathrm{EF}} = c_0. \tag{10}$$

D. Computational method

Finite-element simulations of the continuum model subjected to the Poisson, Nernst-Planck, and Navier-Stokes equations are executed in COMSOL MULTIPHYSICS with its "Electrostatics," "Transport of Diluted Species," and "Laminar Flow" modules, coupled together by the "Multiphysics" module, in the two-dimensional axisymmetric system described in Sec. II. With the dependent variables of the equations required by each other to be solved, as seen in Fig. 1(b) and Eqs. (1)–(10), these predefined modules facilitate their simultaneous solution to be carried out numerically with ease. The fluid and membrane domains are discretized into triangular elements. The mesh is refined adequately near the pore tip H to accurately capture high ionic concentrations, fluid velocities, and electric fields, owing to the large polarization-induced surface charges and strong EDL overlaps in the region. Then, we measure the ionic current through the nanopore as

$$I = \int e(\mathbf{J}_+ - \mathbf{J}_-)\cdot d\mathbf{A}, \tag{11}$$

where $\mathbf{A}$ is a fluid-domain cross-sectional area picked far away from the pore (deep into either reservoir) to obtain

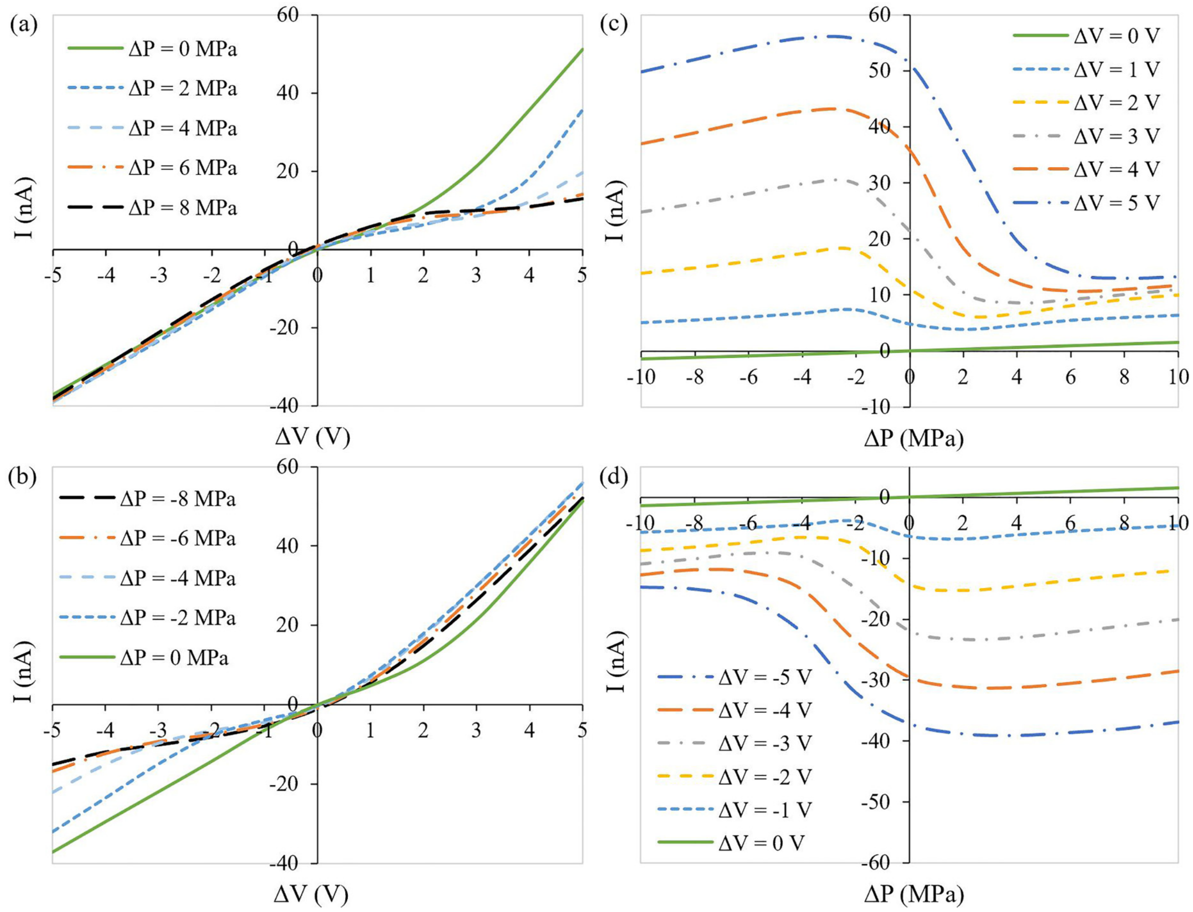

FIG. 2. Current-voltage (*I-V*) plots for the conical nanopore at positive and negative pressures (ΔP) are shown in (a) and (b), respectively, while (c) and (d) illustrate the current-pressure (*I-P*) curves at positive and negative voltages (ΔV), respectively. The simulation parameters used here are the same as in Fig. 1.

precise results. We ensure that the numerical solutions are independent of the effective reservoir dimensions (by sufficiently elongating *DE* and *DC*) and the computational grid.

IV. RESULTS AND DISCUSSION

In this section, we discuss the ion transport features in a conical nanopore with the induced charge effects under a transmembrane electric field and pressure to shed light on the intricate electrohydrodynamic coupling leading to an anomalous variation of the ionic conductance with pressure. To resolve it, we inspect the influence of pressure on the quasiequilibrium ionic concentrations and electric field intensities in the pore, followed by a parametric study to find the conditions that amplify such effects. Lastly, we validate our technique, using it to interpret the pressure-modulated ion transport in other nanochannels. Enroute, we also reveal the mechanism behind the symmetric mechanical activation of ion transport in single-digit CNTs.

A. Electrohydrodynamic (pressure-sensitive) ion transport through the conical nanopore

Figures 1(c) and 1(d) demonstrate the ionic distribution across the nanopore at high voltages, which produce large ICE, when no pressure difference (ΔP) is applied. The negatively charged membrane attracts K^+ (counter)ions and repels Cl^- (co)ions. At positive voltages (ΔV), the downward electric field induces negative charges on *AB* and *AH* [especially near the pore tip *H*, as observed in Fig. 1(e), due to the inevitable reduction in thickness of the membrane near the tip arising from the conical shape of the pore], and positive charges on *HG*, resulting in denser cationic concentrations on *AB* and *AH* compared to *HG* in Fig. 1(c). This is reversed for an upward electric field in Fig. 1(d) under the negative ΔV bias. A strong EDL overlap at the tip end (or orifice) leads to an ICP. At a positive ΔV, the massive accumulation of cations over the sidewall *AH* near the tip *H* attracts large concentrations of anions in the bulk of the orifice. In contrast, the cations gathered below *HG* at negative potentials attract large densities of anions in the vicinity of the orifice but immediately outside the pore. Going forward, this ionic distribution will be critical to interpret the ion transport characteristics in the conical nanopore.

In the absence of pressure, Fig. 2(a) shows a larger current at negative voltages than at a positive ΔV bias when polarization is negligible for low magnitudes of voltage ($\sim$1 V). At a positive ΔV, Cl^- ions moving up are rejected at the orifice outside the pore by the negative surface charges. K^+ ions also accumulate with them on account of electrostatics. This ionic

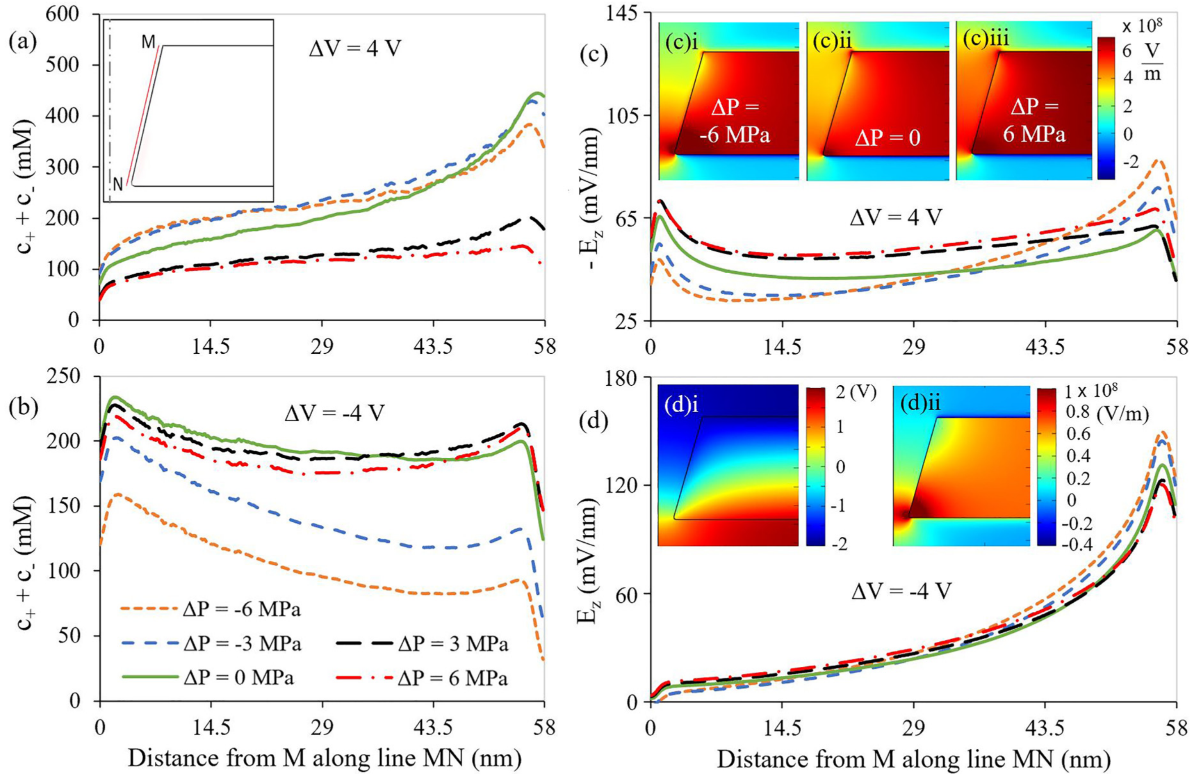

FIG. 3. Total ionic concentrations ($c_+ + c_-$) and axial electric field intensities (E_z) on MN, a line near and parallel to the lateral nanopore surface [see the inset of (a)], are plotted in the left [(a) and (b)] and right [(c) and (d)] panels, respectively, at different pressures (ΔP). The applied voltages (ΔV) in the top [(a) and (c)] and bottom [(b) and (d)] panels are 4 and −4 V, respectively. The 2D contours in the insets of (c) illustrate the electric field intensities in the negative-z direction at $\Delta V = 4$ V as ΔP varies from −6 to 6 MPa. The profiles of electric potential and the electric field intensity in the positive-z direction at $\Delta V = -4$ V in the insets: (d)i and (d)ii, respectively, undergo trivial changes with ΔP. The simulation parameters used are the same as in Fig. 1.

depletion inside the pore reduces the nanopore conductivity. At negative voltages, Cl^- ions enter the pore through its base but cannot permeate the orifice due to electrostatic repulsions. The accumulated Cl^- (and K^+) ions within the pore enhance the conductivity. This leads to the conventional ICR in conical nanopores [31]. However, at larger ΔV magnitudes (∼4 V), an enhanced ICE reverses the ICR [36], as observed in Fig. 2(a). High ionic concentrations within the nanopore near the orifice at positive ΔV [see Figs. 1(c) and 3(a)] in the zone of high electric field intensity [see Fig. 3(c)] produce large currents. Relatively, at negative ΔV, the densities of ions accumulated just outside the nanopore near the orifice [see Figs. 1(d) and 3(b)] in the region of high electric field intensity [see Fig. 3(d)] are way lower [if we compare between Figs. 3(a) and 3(b)], which diminishes the current.

The subsequent exertion of pressure generates an intricate interplay between the mechanical and electrical forces across the nonuniformly charged conical nanopore under the induced charge effects. A hydrodynamic flow shifts the quasiequilibrium positions of the nanopore EDL ions to regions with different electric field intensities (as displayed in Figs. 3 and 4), thus modifying the ionic current in Fig. 2. Therefore, the conical nanopore exhibits a pressure-tuned ionic conductance. The ionic current here can be expressed as a sum of the bare-streaming and electromigration currents,

$$I = \mu(\Delta P) + G(\Delta V) = \mu(\Delta P) + G_0(\Delta V) + G_P(\Delta V), \tag{12}$$

where μ is the bare-streaming mobility and G is the ionic conductance. As G depends on pressure, we separate it into a bare conductance G_0 and a pressure-dependent conductance G_P. The ability of ΔP to distort the nanopore EDL (and affect G_P) depends on the EDL configuration and thus the polarization-induced charges on the nanopore surface, dictated by the polarity and intensity of ΔV. So, G_P, a function of both ΔP and ΔV, represents the electrohydrodynamic coupling in the conical nanopore, while $G_0 = G\,(\Delta V, \Delta P = 0)$ is independent of pressure. As a result, the total streaming current I_str (or the net change in ionic current due to pressure), expressed as

$$I_\mathrm{str} = I(\Delta V, \Delta P) - I(\Delta V, \Delta P = 0) = \mu(\Delta P) + G_P(\Delta V), \tag{13}$$

comprises of two terms, both dictating the pressure sensitivity of ion transport. As the membrane is negatively charged, the excess cations in the solution (to satisfy electroneutrality) when advected by pressure give rise to $\mu(\Delta P)$. ΔV induces equal and opposite charges on the membrane, which does not change the net charge in the fluid. Thus, μ is positive and independent of ΔV.

Figure 2(a) shows that a positive pressure (in the negative-z direction) greatly reduces the current at a positive voltage, also observed in Fig. 2(c). However, it occurs up to a certain limit of pressure beyond which the current starts to rise with ΔP, as shown in Fig. 2(c), and explained later in this section.

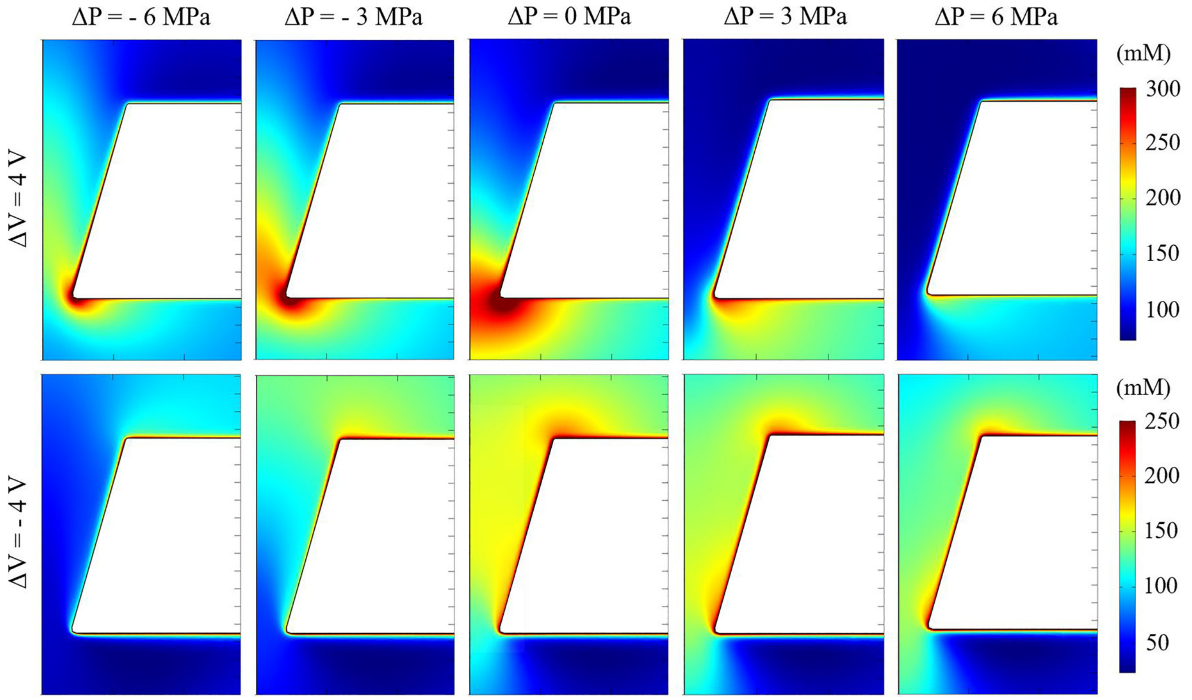

FIG. 4. Two-dimensional contours of the total ionic concentration ($c_+ + c_-$) across the conical nanopore are plotted using the simulation parameters in Fig. 1. The applied pressure (ΔP) varies from -6 to 6 MPa from left to right, while the applied voltage (ΔV) in the top and bottom rows are 4 and -4 V, respectively.

Meanwhile, the significant initial suppression of current due to a pressure applied in the same direction as the electric field contradicts the predictions of the classical linear coupling theory of voltage-driven and streaming ion transport. At $\Delta V = 4$ V and $\Delta P = 0$, the ionic enrichment within the pore orifice [observed in Figs. 1(c) and 3(a)] in the region of high electric field intensity [see Fig. 3(c)] generates a large current. As the right columns of the top row in Fig. 4 illustrate, a downward pressure displaces these ions to quasiequilibrium positions outside the pore where the electric field intensity vanishes. Even if the pressure slightly strengthens the electric field inside the pore [as seen in Fig. 3(c)], the more significant ionic depletion in this once ion-rich region [displayed in Fig. 3(a)] causes the anomalous suppression of ionic current. Besides polarization, the accessibility of the hydrodynamic flow to the ion-enriched zone is also key to attain this electrohydrodynamic coupling generating a negative G_{P}, or an ionic conductance (G) that reduces with pressure applied along the electric field in the converging direction of the conical nanopore.

Conversely, a downward pressure has a trivial influence on the current at negative voltages, as seen in Figs. 2(a) and 2(d). An upward electric field induces positive charges on the pore sidewall to weaken the ionic densities within the nanopore, and negative charges on the membrane's bottom surface (HG) to attract large concentrations of cations below it, as seen in Fig. 1(d). A downward fluid flow (due to a positive ΔP) cannot access (and displace) such cations as the membrane acts as a mechanical barrier. Hence, the density of anions gathered near the orifice outside the pore (due to these cations) is also not affected by positive pressures, as observed in Fig. 3(b). The right columns of the bottom row in Fig. 4 show that ΔP has almost no impact on the ionic concentrations across the nanopore, while Fig. 3(d) displays a trivial influence of ΔP on the electric field profile. Hence, ΔP has a negligible effect on G (i.e., $G_{\mathrm{P}} \sim 0$). Such contrasting effects of the positive pressure on the current at opposite ΔV biases enhance the conventional ICR [31], as demonstrated in Fig. 2(a), which is in complete contrast to the reduction of ICR with ΔP in conical nanopores in the absence of ICE [5–7].

A negative pressure has a relatively small impact on the ionic current at positive voltages and reduces the current magnitude at negative voltages, leading to a nonconventional ICR. A positive ΔV induces an ion-enriched EDL over the pore sidewall. Although an upward fluid motion cannot effectively advect such membrane-shielded ions, as observed in Fig. 3(a), some cations from under the membrane's bottom surface (which has a net negative charge despite a positive charge induction) are pushed into the pore, as shown in the left columns of the top row in Fig. 4, where the electric field intensities are higher. This initially increases the current slightly at positive voltages for negative ΔP in Figs. 2(b) and 2(c), instead of reducing it as expected straightforwardly from Eq. (12). However, as the upward pressure is enlarged, the ions propelled into the pore are pushed out of it through its base, which then reduces the current [as seen in Fig. 2(c)]. A negative ΔV, meanwhile, accumulates cations below the membrane and anions in the bulk just outside the pore orifice, which is also the region of high electric field intensity [see Fig. 3(d)]. An upward fluid flow carries these ions into the nanopore and outside it through the base, as seen in the left columns of the bottom row in Fig. 4, where the electric

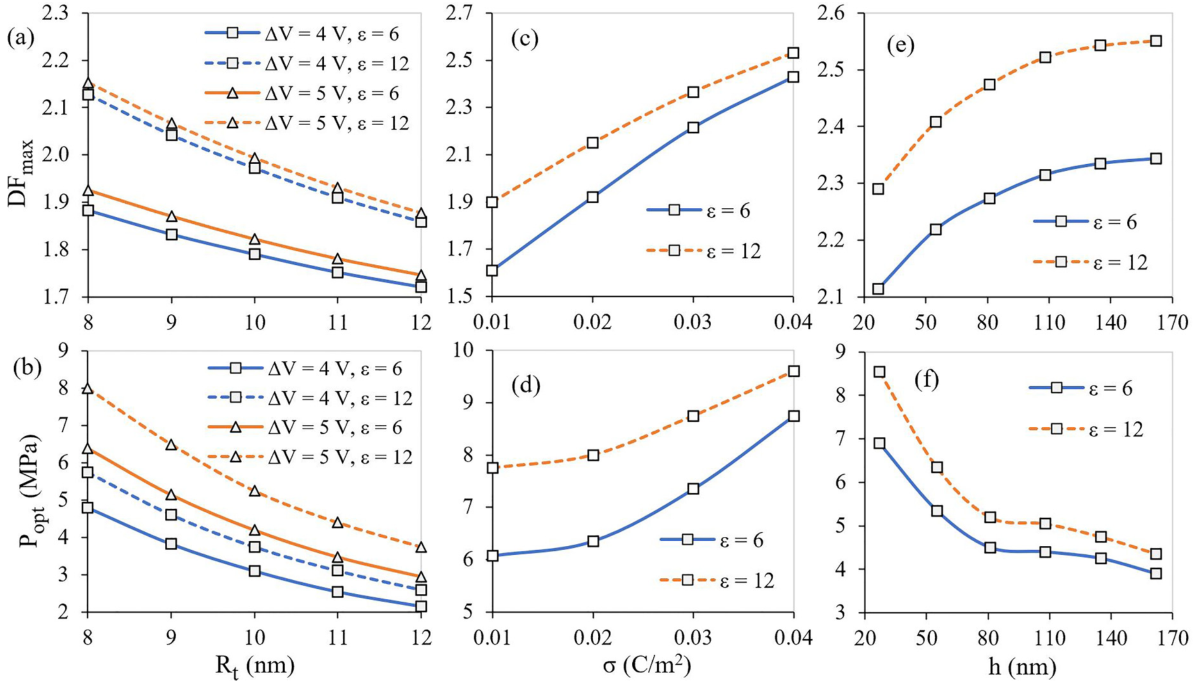

FIG. 5. The effects of the nanopore tip radius (R_t) on the maximum depletion factor ($\mathrm{DF}_{\max}$) and the optimal pressure (P_{opt}) are shown in (a) and (b), respectively, for $\sigma = -0.02\,\mathrm{C/m^2}$ and $h = 55$ nm. The applied voltage (ΔV) and membrane dielectric constant (ε) are simultaneously varied to demonstrate the influence of polarization-induced surface charges. We then plot the effects of the (negative) inherent surface charge density magnitude (σ) on $\mathrm{DF}_{\max}$ and P_{opt} in (c) and (d), respectively, for $h = 55$ nm, $R_t = 8$ nm, $\Delta V = 5$ V, and varying ε. We further illustrate the variations of $\mathrm{DF}_{\max}$ and P_{opt} with the pore length (h) in (e) and (f), respectively, for $\sigma = -0.03\,\mathrm{C/m^2}$, $R_t = 8$ nm, $\Delta V = 4$ V, and different values of ε. We fix θ at 54.7° and c_0 at 100 mM in all the plots of (a)–(f).

fields vanish. As a result, the magnitude of current is initially reduced at a negative ΔV by a negative ΔP in Figs. 2(b) and 2(d), which is again counterintuitive. But, at higher negative ΔP, the current magnitude rises with increasing intensity of pressure, due to the same reason the current at a positive ΔV increases after an initial depletion with positive ΔP, elaborated later in this section.

Therefore, we reveal an anomalous depletion of ionic current when pressure is exerted along the electric field either towards the converging or the diverging end of the conical nanopore. While ΔP generates high fluid velocities along the pore sidewall in the ion-rich EDL when ΔV and ΔP are both positive, it cannot do so in the ion-enriched region below the membrane when ΔV and ΔP are both negative as the membrane acts as a mechanical barrier to the fluid flow. So, the pressure-induced EDL distortion and thus the current suppression is greater when the pressure and electric field both act towards the converging direction of the conical nanopore, evident in Fig. 2. Hence, we mainly focus on this regime to further analyze the electrohydrodynamic coupling in the system.

Figure 2(c), however, shows that the current at $\Delta V > 0$ reduces with increasing positive ΔP only up to a certain limit of pressure, which we explain with Eq. (13). The applied pressure (ΔP), when high, has already displaced a large portion of EDL ions from inside the pore and cannot do so effectively any further. Thus, G_{P} remains negative, but its magnitude drops. Hence, the voltage-driven current $G(\Delta V)$ cannot diminish with ΔP at the same rate, while the bare-streaming current $\mu(\Delta P)$ rises with ΔP. Beyond a certain pressure threshold, which we refer to as the optimal pressure P_{opt}, ΔP affects $\mu(\Delta P)$ more than $G_{\mathrm{P}}(\Delta V)$, thus increasing I_{str} (and I). This mechanism is confirmed by the current-pressure (I-P) curves for varying ΔV at positive ΔP in Fig. 2(c) being almost linear and parallel to the $\Delta V = 0$ curve [where $I = \mu(\Delta P)$] after their minima at $\Delta P = P_{\mathrm{opt}}$. It implies that for $\Delta P > P_{\mathrm{opt}}$, $G(\Delta V)$ is no longer affected by ΔP, and $\mu(\Delta P)$ rises with ΔP at the same rate for all ΔV (as μ is independent of ΔV). Henceforth, we use P_{opt} and the maximum depletion factor $\mathrm{DF}_{\max}$ to mathematically express the electrohydrodynamic behavior in the conical nanopore, where

$$\mathrm{DF}_{\max} = \frac{I(\Delta V, \Delta P = 0)}{I(\Delta V, \Delta P = P_{\mathrm{opt}})} \tag{14}$$

calculates the maximum extent to which the current at a voltage ΔV can be suppressed with pressure. The small values of I in the I-P curve at $\Delta V = 0$ in Fig. 2(c), where $I = \mu(\Delta P)$, relative to those in the curves at $\Delta V \neq 0$, where $I = \mu(\Delta P) + G(\Delta V)$, implies $\mu(\Delta P) \ll G(\Delta V)$. This further simplifies $\mathrm{DF}_{\max}$ to the maximum reduction factor of the ionic conductance (G) with pressure:

$$\begin{aligned}\mathrm{DF}_{\max} &= \frac{\{G(\Delta V, \Delta P = 0)\}\Delta V}{\mu(P_{\mathrm{opt}}) + \{G(\Delta V, \Delta P = P_{\mathrm{opt}})\}\Delta V} \\ &\approx \frac{G(\Delta V, \Delta P = 0)}{G(\Delta V, \Delta P = P_{\mathrm{opt}})}.\end{aligned} \tag{15}$$

A similar reversal in the variation of current is observed at negative ΔV with increasing negative ΔP in Fig. 2(d).

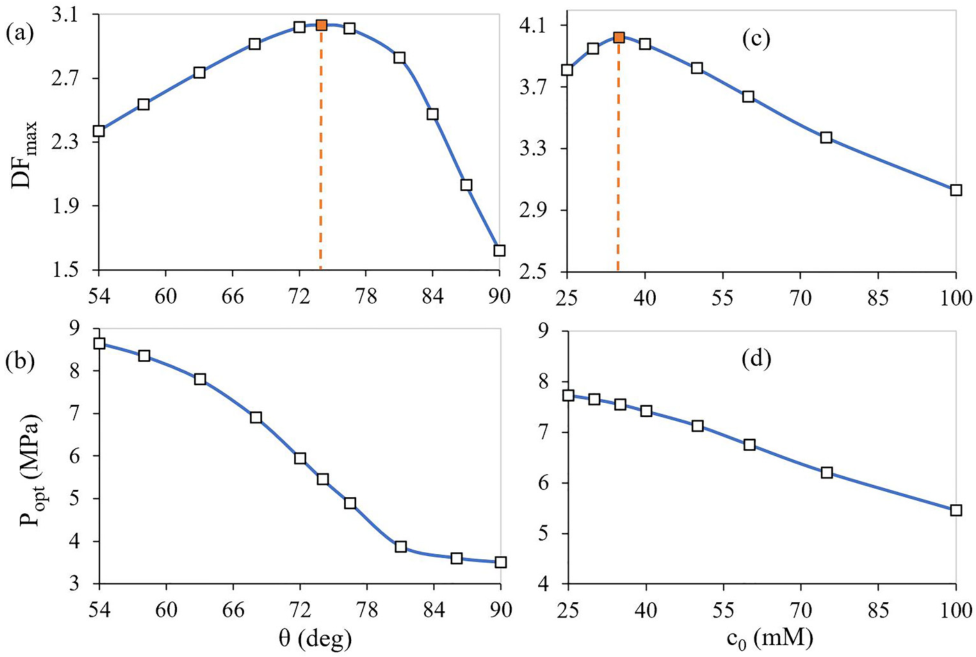

FIG. 6. The effects of the complementary cone angle (θ) on the maximum depletion factor ($\mathrm{DF}_{\max}$) and the optimal pressure (P_{opt}) are plotted in (a) and (b), respectively, for $c_0 = 100$ mM. The variations of $\mathrm{DF}_{\max}$ and P_{opt} with the reservoir salt concentration (c_0) are displayed in (c) and (d), respectively, for $\theta = 74^\circ$. In both sets of plots, we take $\sigma = -0.03\,\mathrm{C/m^2}$, $\varepsilon = 12$, $R_{\mathrm{t}} = 8$ nm, $h = 55$ nm, and $\Delta V = 5$ V. The (orange) shaded data points in (a) and (c) represent the local maxima in the respective curves of $\mathrm{DF}_{\max}$.

The upward pressure initially lowers the current magnitude by displacing the EDL ions away from the pore tip (i.e., the zone of high electric field intensity) to diminish the ionic conductance (G) and thus reduce $|G(\Delta V)|$. After most of the ions are displaced, the effect of ΔP on $G(\Delta V)$ fades and the influence of $\mu(\Delta P)$ starts to dominate, causing the current magnitude to increase.

Interestingly, considering salts like $\mathrm{CaCl_2}$, $\mathrm{Na_2SO_4}$, and $\mathrm{K_2SO_4}$ with ions of varying valences and contrasting diffusion coefficients (unlike KCl) does not alter the ion transport characteristics, as seen in Figs. S1–S3 of the Supplemental Material (SM) [78]. The rest of the results in the study all consider a KCl solution in the system.

B. Enhancement of the pressure sensitivity of ion transport in the conical nanopore

The solid-state conical nanopore displays a pressure-sensitive ion conduction, with a conductance that is suppressed by pressure (under positive ΔV and ΔP). Enhancing this electrohydrodynamic effect requires conditions that promote the ability of the pressure-induced hydrodynamic flow to deform the nanopore EDL at lower magnitudes of pressure, i.e., to enlarge $\mathrm{DF}_{\max}$ and diminish P_{opt}.

A larger R_{t} lowers P_{opt}, as shown in Fig. 5(b), by speeding up the fluid flow. But, it also weakens $\mathrm{DF}_{\max}$, as observed in Fig. 5(a), by effectively pushing the ion-enriched EDL on the pore sidewall away from the peak fluid-flow zone in the bulk. Higher net surface charge densities, either due to σ or ICE (via ε or ΔV), amplify the amount of EDL ions that can be displaced by pressure, which raises both $\mathrm{DF}_{\max}$ and P_{opt}, as demonstrated throughout Fig. 5. Thicker membranes (due to higher h) magnify $\mathrm{DF}_{\max}$, as seen in Fig. 5(e), by reducing the EDL ion overspill into the reservoirs through enlarged lateral confinements of the pore at $\Delta P = 0$ [79]. A longer nanopore further reduces P_{opt} in Fig. 5(f) due to higher fluid velocities at wider average pore cross sections (as θ is kept constant).

A larger θ steepens the lateral surface of the conical nanopore, thus raising the component of fluid velocity along it. This lowers P_{opt} [see Fig. 6(b)] and initially elevates $\mathrm{DF}_{\max}$ [see Fig. 6(a)]. But, as we approach towards a cylindrical nanopore, a rising θ also reduces the component of the pore-sidewall area normal to the external electric field and thus the amount of EDL ions to be dislodged by pressure (as ICE becomes negligible). Hence, $\mathrm{DF}_{\max}$ starts to diminish, resulting in a maximum in the $\mathrm{DF}_{\max}$-θ curve at an intermediate θ ($= 74^\circ$) in Fig. 6(a). In concentrated electrolytes (at higher c_0), the counterions shield the nanopore surface charges more efficiently to reduce both $\mathrm{DF}_{\max}$ and P_{opt} in Figs. 6(c) and 6(d), respectively, agreeing with the effects of reducing σ. However, if the solution is diluted beyond a certain limit [35 mM, as shown in Fig. 6(c)], $\mathrm{DF}_{\max}$ is lowered instead of increasing due to a lack of ions in the EDL that can be displaced, leading to a maximum in the $\mathrm{DF}_{\max} - c_0$ plot. Hence, tuning the pressure sensitivity of ion transport depends on the confluence of all these factors.

C. General framework to study nanoscale electrohydrodynamic ion transport

To explain the electrohydrodynamic coupling in our apparatus, (i) we realized the regions of large ionic accumulations and electric field intensities before applying pressure; (ii) We

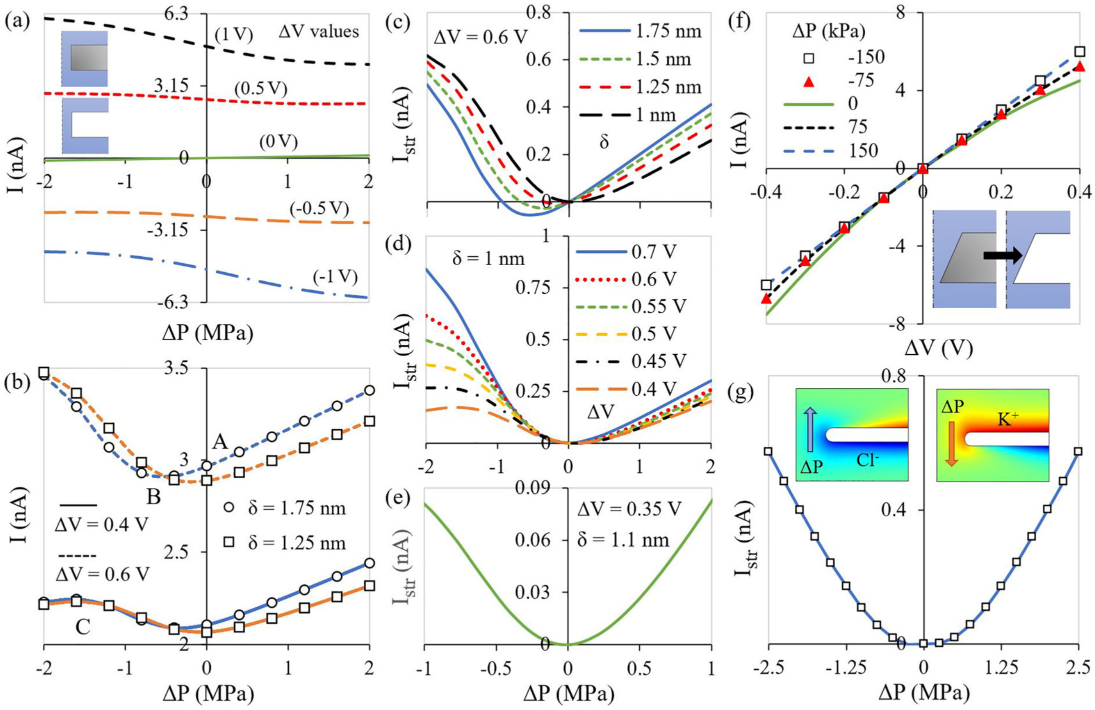

FIG. 7. (a) Current-pressure (*I-P*) curves are plotted for a cylindrical nanopore ($\theta = 90^\circ$) with $\sigma = -0.03\,\mathrm{C/m^2}$, $\varepsilon = 12$, $R_t = 8$ nm, $h = 55$ nm, $c_0 = 100$ mM, and $\delta = 0$. Here, the (black) dashed, (red) square-dotted, (green) solid, (orange) long-dashed, and (blue) dashed-dotted lines correspond to the ΔV values of 1, 0.5, 0, -0.5, and -1 V, respectively. The subsequent consideration of $\delta \neq 0$ yields nonmonotonic *I-P* plots in (b) and the associated streaming current vs pressure (I_{str}-*P*) plots in (c)–(e). The horizontal axes of (c) and (d) have identical limits. (f) Current-voltage curves for a conical nanopore without a membrane domain are plotted at varying pressures (ΔP) with $\sigma = -0.026\,\mathrm{C/m^2}$, $R_t = 185$ nm, $h = 20\,\mu$m, $\theta = 80^\circ$, and $c_0 = 10$ mM. (g) I_{str}-*P* plots for a graphene nanopore with $\sigma = 0$, $\varepsilon = 3$, $R_t = 1.16$ nm, $h = 0.34$ nm, $c_0 = 1$ M, $\Delta V = 100$ mV, $D(\mathrm{K^+}) = 1.45 \times 10^{-9}\,\mathrm{m^2/s}$, $D(\mathrm{Cl^-}) = 1.51 \times 10^{-9}\,\mathrm{m^2/s}$, and slip velocities on the membrane surfaces (detailed in Sec. IV of the Supplemental Material [78]). The left and right insets in (g) demonstrate the impact of negative and positive ΔP on the net ionic concentrations ($c_+ - c_-$) near the pore opening, respectively.

then probed the influence of pressure on the ionic concentrations in these regions (and thus on the conductance); and (iii) The resultant variation in voltage-driven current was appended to that of the (bare-)streaming current, to gauge the net effect of applied pressure on ionic current. Now, we use this approach for qualitatively characterizing the electrohydrodynamic ion conduction in different nanochannels to delineate the dramatic change in the pressure sensitivity of ion transport with the channel geometry and due to various physics.

To mimic the electrohydrodynamic ion transport in CNTs [3], we take $\theta = 90^\circ$ to modify the channel to a cylindrical nanopore and apply a hydrodynamic slip on its lateral surface (AH) using a slip length of δ. At $\theta = 90^\circ$ and $\delta = 0$, the *I-P* curves in Fig. S5 of SM [78] display a reduction of current with pressure when ΔV and ΔP are parallel, similar to that of the conical nanopore in Figs. 2(c) and 2(d). We further lower the ranges of ΔV and ΔP across the cylindrical nanopore in the *I-P* curves of Fig. 7(a), in accordance with the magnitudes of electromechanical forces usually applied across CNTs to study ion transport [3], which exhibit a similar suppression of current with pressure. This is again caused due to the pressure-induced depletion of ionic concentrations in the zone of high electric field intensity, as shown in Figs. S6 and S7 of SM [78]. However, the current depletions in both Figs. 7(a) and S5 [78] are small compared to that in Figs. 2(c) and 2(d) due to the absence of large induced charges on the lateral nanopore surface (as it is now parallel to the external electric field), explaining the significance of the ICE due to membrane polarization towards the strong pressure-induced suppression of ionic current across a solid-state conical nanopore. This is further confirmed when the exact same $I - P$ curves in Figs. 7(a) and S5 (of SM [78]) are obtained using a numerical model of the cylindrical nanopore without considering the membrane domain (see Fig. S4 of SM [78]). Moreover, in the planar (Cartesian) analogs of these nanopores, i.e., tapered and rectangular nanoslits (see Figs. S8 and S9 of SM [78]), the presence and absence of ICE cause their *I-P* curves to be similar to those of the conical and cylindrical nanopores, respectively.

However, introducing a hydrodynamic slip on the lateral surface of the pore (such as in a CNT) yields a nonmonotonous behavior of the current with pressure in Fig. 7(b) due to a manifold rise in the hydrodynamic flow and thus the (bare-)streaming current $\mu(\Delta P)$. The current now rises with pressure at positive ΔP as the increase in $\mu(\Delta P)$ outweighs the reduction of $G_{\mathrm{P}}(\Delta V)$ with ΔP. This rise in current actually starts at $\Delta P < 0$ due to the positive streaming current of the excess $\mathrm{K^+}$ ions caused by the slip-enhanced downward electro-osmotic flow (EOF) at positive ΔV. A positive *I-P* slope at point A verifies that. However, a negative ΔP

nullifies the downward EOF and also the streaming current it generated. Hence, $G_{\mathrm{P}}(\Delta V)$ dominates $\mu(\Delta P)$ and I reduces with increasing ΔP, like in the *I-P* curves for $\Delta V > 0$ in Fig. 7(a), to yield a minimum at point B. Meanwhile, a larger negative pressure again causes the effects of $\mu(\Delta P)$ to eclipse those of $G_{\mathrm{P}}(\Delta V)$, reducing I beyond the maxima at point C. Figures S10 and S11 of SM [78] show a symmetric pressure-induced distortion of the nanopore EDL and $I(\Delta V, \Delta P) = -I(-\Delta V, -\Delta P)$ due to the symmetric shape of the cylindrical nanopore. As the hydrodynamic slip length (δ) is increased in Fig. 7(b), the EOF is accelerated at $\Delta P = 0$, which raises I at point A owing to the enhanced net-counterionic advection. It now requires a greater negative pressure to cancel the EOF, shifting both points B and C to the left. A larger positive ΔV has the same effects on the points A, B, and C, as it also magnifies the EOF.

In the resultant streaming current vs pressure (I_{str}-P) curves in Figs. 7(c)–7(e), the nonmonotonic responses of the streaming current to pressure are usually not symmetric [as the point B in Fig. 7(b) does not lie on the $\Delta P = 0$ axis, shifting with δ and ΔV]. However, for certain $\Delta V - \delta$ combinations, such as in Fig. 7(e), a perfectly symmetric nonlinear pressure dependence of the streaming current is exhibited, similar to the symmetric (near-quadratic) activation of streaming current with applied pressure in single-digit CNTs obtained by Marcotte *et al.* [3]. Therefore, we are able to disentangle the electrohydrodynamic coupling in narrow CNTs by analyzing the interplay between the effects of pressure on the (bare-)streaming current (originating from the hydrodynamic transport of ions) and the electromigration current. This is significant as, albeit Marcotte *et al.* presented a meticulous mathematical explanation for the approximate quadratic enhancement of the streaming current in a narrow CNT with pressure [3], the underlying physical mechanism behind the phenomenon had so far remained elusive.

We also simulate the ion transport in a conical nanopore under an electric field and pressure in the absence of ICE [5] in Fig. 7(f) by disregarding the membrane domain (see Fig. S12 of SM [78]). At $\Delta P = 0$, negative-ΔV biases generate larger currents, which is the conventional ICR in a conical nanopore [5–7], due to the enrichment (depletion) of ions inside the pore under a negative (positive) voltage (explained in Sec. IV A). However, a pressure exerted in either direction forces the neutral bulk concentration of ions from the reservoirs into the nanopore, as observed in Fig. S13 of SM [78]. This negates the ICP within the pore in the opposite ΔV biases that existed prior to the application of pressure, therefore nullifying the ICR, in sheer contrast to the results of Figs. 2(a) and 2(b), where an applied pressure in either direction along the conical nanopore enhances ICR under the presence of ICE.

Finally, we shrink the pore length (h) to the diameter of a carbon atom (in Fig. S14 of SM [78]) to yield the pressure-sensitive ion transport in graphene nanopores [4]. We set hydrodynamic slip velocities on the pore and membrane surfaces (detailed in Sec. IV of SM [78]) to replicate the fluid velocities near the pore opening obtained by Jiang *et al.* [4]. Albeit Fig. 7(g) does not display the exact expected linear increase of the streaming current with pressure, we still mimic the symmetric I_{str}-P relation exhibited in graphene nanopores [4]. This behavior is again justified by the effect of pressure on the ionic distribution near the pore in Fig. S15 of SM [78]. Cations (anions) accumulate on the membrane surface near the positive (negative) electrode simply due to a voltage bias, which is further enhanced by ICE. A pressure applied towards the negative (positive) electrode displaces the cations (anions) closer to the pore opening, owing to the high hydrodynamic slip on graphene, which makes them easier to be pushed by the transmembrane electric field, thus increasing the ionic conductance. Figure S16 of SM [78] illustrates $I(\Delta V, \Delta P) = -I(-\Delta V, -\Delta P)$ again due to the symmetric channel shape. The effects of $\mu(\Delta P)$ are not observed here as we consider $\sigma = 0$.

Hence, we underline that analyzing how the quasiequilibrium distribution of EDL ions changes under hydrodynamic flows and its resultant effect on the ionic conductance serves as a fundamental technique to predict the ion transport under combined electrical and mechanical forcing in different nanochannels and in various physical regimes. Accounting for the ionic current due to the advection of ions either by pressure-driven or electro-osmotic fluid flows, denoted by the bare-streaming current in our analysis, is also essential to the process. However, we fail to study the mechanism behind the electrohydrodynamic ion transport characteristics in 0.67-nm-wide (angstrom-scale) graphene slits demonstrated experimentally by Mouterde *et al.* [2], as our continuum model cannot capture molecular-level physics. Yet, if studied using molecular dynamics (MD) simulations, it is possible that the simultaneous influence of voltage and pressure on the two-dimensional ionic distribution across the slit (which cannot be revealed by one-dimensional COMSOL simulations, as attempted by Mouterde *et al.* [2]) will hold the key to a more explicit reasoning behind their observations.

V. CONCLUSION

In this paper, the ion transport through a truncated-conical nanopore embedded within a dielectric membrane between two reservoirs filled with an electrolyte solution was studied under an electric field and pressure. We highlighted the significance of induced charge effects in solid-state conical nanopores due to the extremely low membrane thickness near the pore tip. The ion transport was solved by numerical simulations of a continuum model based on the Poisson, Nernst-Planck, and Navier-Stokes equations because using MD to account for the polarization-induced surface charges adds inordinate complexity to the analysis and is extremely challenging in terms of computational time.

We revealed an anomalous electrohydrodynamic coupling that suppresses ionic current when pressure is applied along the electric field, especially if both act towards the converging direction of the conical nanopore, which opposes the classical linear coupling theory of voltage-driven and streaming ion transport. It also enhances the rectification of ionic current with an applied pressure, thoroughly contradicting the findings of previous investigations. We demonstrated that membrane polarization is crucial to attain such a counterintuitive pressure sensitivity of ion transport while exploring the conditions that amplify it. Contrasting nonuniform nanopore EDLs are generated at opposite electric field polarities, while the skewed nanopore geometry renders varying extents of protection to the EDL ions against hydrodynamic dislocation for opposite directions of applied pressure. This complex electromechanical interplay determines the overall nature and intensity of the pressure modulation of ion conduction in solid-state conical nanopores.

We thereafter showed that inspecting the hydrodynamic disruption to the quasisteady state of the channel EDL, followed by the resultant balance between the pressure-induced changes in the electromigration current and the current due to the hydrodynamic streaming of ions, can also clarify the pressure-sensitive ion transport in carbon nanotubes, graphene nanopores, and nonpolarizable conical nanopores. Hence, we propose this approach as a fundamental method to predict or explain the electrohydrodynamic ion transport characteristics in a wide array of nanoconduits and under the influence of different physical effects, whether probed under continuum-based computational models or MD simulations. We expect this analysis to enhance our grasp over the electrokinetic responses in nanoconfinements to external electrical and mechanical stimuli, paving the way to design nanofluidic devices with routes toward more modular, tunable, and robust control of molecular, fluid, and ion transport. Besides finding applications such as building ionic circuits, exploiting the magnified polarization and geometry-related effects in our system to boost the ion-selectivity and biosensing abilities of nanopores must be considered for future research.

ACKNOWLEDGMENTS

This study was supported by the Center for Enhanced Nanofluidic Transport (CENT), an Energy Frontier Research Center funded by the U.S. Department of Energy, Office of Science, Basic Energy Sciences (Award No. DE-SC0019112), and the National Science Foundation under Grants No. 2140225 and No. 2137157. The computing power was provided by the Extreme Science and Engineering Discovery Environment (XSEDE) granted by National Science Foundation (NSF) Grant No. OCI1053575 and Blue Waters supercomputing center, awarded by the state of Illinois and NSF Grants No. OCI-0725070 and No. ACI-1238993. A.P. performed simulations, analysis, and wrote the manuscript under the guidance of N.R.A.

---

[1] L. Bocquet and E. Charlaix, Nanofluidics, from bulk to interfaces, Chem. Soc. Rev. **39**, 1073 (2010).

[2] T. Mouterde, A. Keerthi, A. R. Poggioli, S. A. Dar, A. Siria, A. K. Geim, L. Bocquet, and B. Radha, Molecular streaming and its voltage control in ångström-scale channels, Nature (London) **567**, 87 (2019).

[3] A. Marcotte, T. Mouterde, A. Niguès, A. Siria, and L. Bocquet, Mechanically activated ionic transport across single-digit carbon nanotubes, Nat. Mater. **19**, 1057 (2020).

[4] X. Jiang, C. Zhao, Y. Noh, Y. Xu, Y. Chen, F. Chen, L. Ma, W. Ren, N. R. Aluru, and J. Feng, Nonlinear electrohydrodynamic ion transport in graphene nanopores, Sci. Adv. **8**, eabj2510 (2022).

[5] W. J. Lan, D. A. Holden, and H. S. White, Pressure-dependent ion current rectification in conical-shaped glass nanopores, J. Am. Chem. Soc. **133**, 13300 (2011).

[6] X. R. Zhu, L. Wang, C. M. Wang, Z. Jiao, W. D. Wang, G. Y. Qin, and J. M. Xue, Pressure-dependent electrolytic conduction of track-etched single conical nanopore, Appl. Surf. Sci. **353**, 574 (2015).

[7] L. Jubin, A. Poggioli, A. Siria, and L. Bocquet, Dramatic pressure-sensitive ion conduction in conical nanopores, Proc. Natl. Acad. Sci. USA **115**, 4063 (2018).

[8] A. Anishkin, S. H. Loukin, J. Teng, and C. Kung, Feeling the hidden mechanical forces in lipid bilayer is an original sense, Proc. Natl. Acad. Sci. USA **111**, 7898 (2014).

[9] C. D. Cox, N. Bavi, and B. Martinac, Biophysical principles of ion-channel-mediated mechanosensory transduction, Cell Rep. **29**, 1 (2019).

[10] B. Coste *et al.*, Piezo proteins are pore-forming subunits of mechanically activated channels, Nature (London) **483**, 176 (2012).

[11] S.-H. Chung, O. S. Andersen, and V. Krishnamurthy, *Biological Membrane Ion Channels: Dynamics, Structure, and Applications* (Springer Science & Business Media, New York, 2007).

[12] L. Bocquet, Nanofluidics coming of age, Nat. Mater. **19**, 254 (2020).

[13] S. Faucher *et al.*, Critical knowledge gaps in mass transport through single-digit nanopores: A review and perspective, J. Phys. Chem. C **123**, 21309 (2019).

[14] R. H. Tunuguntla, R. Y. Henley, Y.-C. Yao, T. A. Pham, M. Wanunu, and A. Noy, Enhanced water permeability and tunable ion selectivity in subnanometer carbon nanotube porins, Science **357**, 792 (2017).

[15] M. I. Walker, K. Ubych, V. Saraswat, E. A. Chalklen, P. Braeuninger-Weimer, S. Caneva, R. S. Weatherup, S. Hofmann, and U. F. Keyser, Extrinsic cation selectivity of 2D membranes, ACS Nano **11**, 1340 (2017).

[16] H. Y. Yang, Z. J. Han, S. F. Yu, K. L. Pey, K. Ostrikov, and R. Karnik, Carbon nanotube membranes with ultrahigh specific adsorption capacity for water desalination and purification, Nat. Commun. **4**, 2220 (2013).

[17] J. Feng, K. Liu, M. Graf, D. Dumcenco, A. Kis, M. di Ventra, and A. Radenovic, Observation of ionic coulomb blockade in nanopores, Nat. Mater. **15**, 850 (2016).

[18] R. K. Joshi, P. Carbone, F. C. Wang, V. G. Kravets, Y. Su, I. v. Grigorieva, H. A. Wu, A. K. Geim, and R. R. Nair, Precise and ultrafast molecular sieving through graphene oxide membranes, Science **343**, 752 (2014).

[19] Q. Xie, M. A. Alibakhshi, S. Jiao, Z. Xu, M. Hempel, J. Kong, H. G. Park, and C. Duan, Fast water transport in graphene nanofluidic channels, Nat. Nanotechnol. **13**, 238 (2018).

[20] A. Paul and N. R. Aluru, Nonlocal hydrodynamic model for gravity-driven transport in nanochannels, J. Chem. Phys. **156**, 204112 (2022).

[21] N. R. Aluru *et al.*, Fluids and electrolytes under confinement in single-digit nanopores, ACS Chem. Rev. **123**, 2737 (2022).

[22] B. Radha *et al.*, Molecular transport through capillaries made with atomic-scale precision, Nature (London) **538**, 222 (2016).

[23] A. Esfandiar, B. Radha, F. C. Wang, Q. Yang, S. Hu, S. Garaj, R. R. Nair, A. K. Geim, and K. Gopinadhan, Size effect in ion transport through angstrom-scale slits, Science **358**, 511 (2017).

[24] F. Fornasiero, H. G. Park, J. K. Holt, M. Stadermann, P. Grigoropoulos, A. Noy, and O. Bakajin, Ion exclusion by sub-2-nm carbon nanotube pores, Proc. Natl. Acad. Sci. USA **105**, 17250 (2008).

[25] A. Siria, P. Poncharal, A. L. Biance, R. Fulcrand, X. Blase, S. T. Purcell, and L. Bocquet, Giant osmotic energy conversion measured in a single transmembrane boron nitride nanotube, Nature (London) **494**, 455 (2013).

[26] J. Feng, M. Graf, K. Liu, D. Ovchinnikov, D. Dumcenco, M. Heiranian, V. Nandigana, N. R. Aluru, A. Kis, and A. Radenovic, Single-layer MoS_2 nanopores as nanopower generators, Nature (London) **536**, 197 (2016).

[27] T. Jain, B. C. Rasera, R. J. S. Guerrero, M. S. H. Boutilier, S. C. O'Hern, J. C. Idrobo, and R. Karnik, Heterogeneous sub-continuum ionic transport in statistically isolated graphene nanopores, Nat. Nanotechnol. **10**, 1053 (2015).

[28] J. Abraham *et al.*, Tunable sieving of ions using graphene oxide membranes, Nat. Nanotechnol. **12**, 546 (2017).

[29] H. Zhang, X. Hou, J. Hou, L. Zeng, Y. Tian, L. Li, and L. Jiang, Synthetic asymmetric-shaped nanodevices with symmetric PH-gating characteristics, Adv. Funct. Mater. **25**, 1102 (2015).

[30] M. Ali, B. Yameen, J. Cervera, P. Ramírez, R. Neumann, W. Ensinger, W. Knoll, and O. Azzaroni, Layer-by-layer assembly of polyelectrolytes into ionic current rectifying solid-state nanopores: Insights from theory and experiment, J. Am. Chem. Soc. **132**, 8338 (2010).

[31] Z. S. Siwy, Ion-current rectification in nanopores and nanotubes with broken symmetry, Adv. Funct. Mater. **16**, 735 (2006).

[32] Z. Siwy, E. Heins, C. C. Harrell, P. Kohli, and C. R. Martin, Conical-nanotube ion-current rectifiers: The role of surface charge, J. Am. Chem. Soc. **126**, 10850 (2004).

[33] L. Cao, W. Guo, Y. Wang, and L. Jiang, Concentration-gradient-dependent ion current rectification in charged conical nanopores, Langmuir **28**, 2194 (2012).

[34] J. Wei, G. Du, J. Guo, Y. Li, W. Liu, H. Yao, J. Zhao, R. Wu, H. Chen, and A. Ponomarov, The rectification of mono- and bivalent ions in single conical nanopores, Nucl. Instrum. Methods Phys. Res. B **404**, 219 (2017).

[35] S. Tseng, S. C. Lin, C. Y. Lin, and J. P. Hsu, Influences of cone angle and surface charge density on the ion current rectification behavior of a conical nanopore, J. Phys. Chem. C **120**, 25620 (2016).

[36] Y. Yao, C. Wen, N. H. Pham, and S. L. Zhang, On induced surface charge in solid-state nanopores, Langmuir **36**, 8874 (2020).

[37] B. Zhang, Y. Ai, J. Liu, S. W. Joo, and S. Qian, Polarization effect of a dielectric membrane on the ionic current rectification in a conical nanopore, J. Phys. Chem. C **115**, 24951 (2011).

[38] C. Wen, S. Zeng, S. Li, Z. Zhang, and S. L. Zhang, On rectification of ionic current in nanopores, Anal. Chem. **91**, 14597 (2019).

[39] B. Yameen, M. Ali, R. Neumann, W. Ensinger, W. Knoll, and O. Azzaroni, Single conical nanopores displaying PH-tunable rectifying characteristics. manipulating ionic transport with zwitterionic polymer brushes, J. Am. Chem. Soc. **131**, 2070 (2009).

[40] J. Cervera, B. Schiedt, R. Neumann, S. Mafá, and P. Ramírez, Ionic conduction, rectification, and selectivity in single conical nanopores, J. Chem. Phys. **124**, 104706 (2006).

[41] Y. Zhang and G. C. Schatz, Conical nanopores for efficient ion pumping and desalination, J. Phys. Chem. Lett. **8**, 2842 (2017).

[42] C. Dekker, Solid-state nanopores, Nat. Nanotechnol. **2**, 209 (2007).

[43] W. Guo, Y. Tian, and L. Jiang, Asymmetric ion transport through ion-channel-mimetic solid-state nanopores, Acc. Chem. Res. **46**, 2834 (2013).

[44] K. Xiao, L. Wen, and L. Jiang, Biomimetic solid-state nanochannels: From fundamental research to practical applications, Small **12**, 2810 (2016).

[45] S. Ghosal, J. D. Sherwood, and H. C. Chang, Solid-state nanopore hydrodynamics and transport, Biomicrofluidics **13**, 011301 (2019).

[46] F. Haque, J. Li, H. C. Wu, X. J. Liang, and P. Guo, Solid-state and biological nanopore for real-time sensing of single chemical and sequencing of DNA, Nano Today **8**, 56 (2013).

[47] C. Wang, Q. Fu, X. Wang, D. Kong, Q. Sheng, Y. Wang, Q. Chen, and J. Xue, Atomic layer deposition modified track-etched conical nanochannels for protein sensing, Anal. Chem. **87**, 8227 (2015).

[48] U. F. Keyser, B. N. Koeleman, S. van Dorp, D. Krapf, R. M. M. Smeets, S. G. Lemay, N. H. Dekker, and C. Dekker, Direct force measurements on DNA in a solid-state nanopore, Nat. Phys. **2**, 473 (2006).

[49] D. Branton *et al.*, The potential and challenges of nanopore sequencing, Nat. Biotechnol. **26**, 1146 (2008).

[50] A. P. Ivanov, E. Instuli, C. M. McGilvery, G. Baldwin, D. W. McComb, T. Albrecht, and J. B. Edel, DNA tunneling detector embedded in a nanopore, Nano Lett. **11**, 279 (2011).

[51] B. M. Venkatesan and R. Bashir, Nanopore sensors for nucleic acid analysis, Nat. Nanotechnol. **6**, 615 (2011).

[52] W. L. Hsu and H. Daiguji, Manipulation of protein translocation through nanopores by flow field control and application to nanopore sensors, Anal. Chem. **88**, 9251 (2016).

[53] S. Zeng, C. Wen, P. Solomon, S. L. Zhang, and Z. Zhang, Rectification of protein translocation in truncated pyramidal nanopores, Nat. Nanotechnol. **14**, 1056 (2019).

[54] E. C. Yusko *et al.*, Real-time shape approximation and fingerprinting of single proteins using a nanopore, Nat. Nanotechnol. **12**, 360 (2017).

[55] L. Restrepo-Pérez, C. Joo, and C. Dekker, Paving the way to single-molecule protein sequencing, Nat. Nanotechnol. **13**, 786 (2018).

[56] J. J. Kasianowicz, E. Brandin, D. Branton, and D. W. Deamer, Characterization of individual polynucleotide molecules using a membrane channel, Proc. Natl. Acad. Sci. U.S.A. **93**, 13770 (1996).

[57] A. Meller, L. Nivon, and D. Branton, Voltage-driven DNA translocations through a nanopore, Phys. Rev. Lett. **86**, 3435 (2001).

[58] Y. Ai and S. Qian, Electrokinetic particle translocation through a nanopore, Phys. Chem. Chem. Phys. **13**, 4060 (2011).

[59] F. Montagne, N. Blondiaux, A. Bojko, and R. Pugin, Molecular transport through nanoporous silicon nitride membranes produced from self-assembling block copolymers, Nanoscale **4**, 5880 (2012).

[60] M. L. Kovarik and S. C. Jacobson, Nanofluidics in lab-on-a-chip devices, Anal. Chem. **81**, 7133 (2009).

[61] T. Z. Jubery, A. S. Prabhu, M. J. Kim, and P. Dutta, Modeling and simulation of nanoparticle separation through a solid-state nanopore, Electrophoresis **33**, 325 (2012).

[62] S. J. Kim, Y. C. Wang, J. H. Lee, H. Jang, and J. Han, Concentration polarization and nonlinear electrokinetic flow near a nanofluidic channel, Phys. Rev. Lett. **99**, 044501 (2007).

[63] T. A. Zangle, A. Mani, and J. G. Santiago, Theory and experiments of concentration polarization and ion focusing at microchannel and nanochannel interfaces, Chem. Soc. Rev. **39**, 1014 (2010).

[64] L. H. Yeh, M. Zhang, S. Qian, J. P. Hsu, and S. Tseng, Ion concentration polarization in polyelectrolyte-modified nanopores, J. Phys. Chem. C **116**, 8672 (2012).

[65] L. H. Yeh, M. Zhang, and S. Qian, Ion transport in a PH-regulated nanopore, Anal. Chem. **85**, 7527 (2013).

[66] H. C. Yeh, C. C. Chang, and R. J. Yang, Electro-osmotic pumping and Ion-concentration polarization based on conical nanopores, Phys. Rev. E **91**, 062302 (2015).

[67] I. Vlassiouk, S. Smirnov, and Z. Siwy, Ionic selectivity of single nanochannels, Nano Lett. **8**, 1978 (2008).

[68] Z. Siwy, I. D. Kosińska, A. Fuliński, and C. R. Martin, Asymmetric diffusion through synthetic nanopores, Phys. Rev. Lett. **94**, 048102 (2005).

[69] P. Ramírez, V. Gómez, J. Cervera, B. Schiedt, and S. Mafé, Ion transport and selectivity in nanopores with spatially inhomogeneous fixed charge distributions, J. Chem. Phys. **126**, 194703 (2007).

[70] M. Z. Bazant and T. M. Squires, Induced-charge electrokinetic phenomena: Theory and microfluidic applications, Phys. Rev. Lett. **92**, 066101 (2004).

[71] S. M. Davidson, M. B. Andersen, and A. Mani, Chaotic induced-charge electro-osmosis, Phys. Rev. Lett. **112**, 128302 (2014).

[72] G. Yossifon, I. Frankel, and T. Miloh, Symmetry breaking in induced-charge electro-osmosis over polarizable spheroids, Phys. Fluids **19**, 068105 (2007).

[73] D. Saintillan, E. Darve, and E. S. G. Shaqfeh, Hydrodynamic interactions in the induced-charge electrophoresis of colloidal rod dispersions, J. Fluid Mech. **563**, 223 (2006).

[74] M. Z. Bazant and T. M. Squires, Induced-charge electrokinetic phenomena, Curr. Opin. Colloid Interface Sci. **15**, 203 (2010).

[75] T. M. Squires, Induced-charge electrokinetics: Fundamental challenges and opportunities, Lab Chip **9**, 2477 (2009).

[76] J. P. de Souza, C. M. Chow, R. Karnik, and M. Z. Bazant, Nonlinear ion transport mediated by induced charge in ultrathin nanoporous membranes, Phys. Rev. E **104**, 044802 (2021).

[77] J. D. Sherwood, M. Mao, and S. Ghosal, Electroosmosis in a finite cylindrical pore: Simple models of end effects, Langmuir **30**, 9261 (2014).

[78] See Supplemental Material at http://link.aps.org/supplemental/10.1103/PhysRevE.109.025105 for additional details and figures that aid the discussions in this paper, mostly with the results in Sec. IV C.

[79] A. Paul, S. Mukherjee, J. Dhar, S. Ghosal, and S. Chakraborty, The effect of the finite size of ions and debye layer overspill on the screened coulomb interactions between charged flat plates, Electrophoresis **41**, 607 (2020).